Computational method for high resolution spectral analysis of fractionated atrial electrograms

Edward J. Ciaccio*, Angelo B. Biviano, Hasan Garan

Department of Medicine—Division of Cardiology Columbia University Medical Center, 630 West 168th Street, New York, NY, USA

ABSTRACT

Background: The discrete Fourier transform (DFT) is often used as a spectral estimator for analysis of complex fractionated atrial electrograms (CFAE) acquired during atrial fibrillation (AF). However, time resolution can be unsatisfactory, as the frequency resolution is proportional to rate/time interval. In this study we compared the DFT to a new spectral estimator with improved time-frequency resolution.
Method: Recently, a novel spectral estimator (NSE) based upon signal averaging was derived and implemented computationally. The NSE is similar to the DFT in that both estimators model the autocorrelation function to form the power spectrum. However, as derived in this study, NSE frequency resolution is proportional to $rate/period^2$ and thus unlike the DFT, is not directly dependent on the window length. We hypothesized that the NSE would provide improved time resolution while maintaining satisfactory frequency resolution for computation of CFAE spectral parameters. Window lengths of 8 s, 4 s, 2 s, 1 s, and 0.5 s were used for analysis. Two criteria gauged estimator performance. Firstly, a periodic electrogram pattern with phase jitter was embedded in interference. The error in detecting the frequency of the periodic pattern was determined. Secondly, significant differences in spectral parameters for paroxysmal versus persistent AF data, which have known dissimilarities, were determined using the DFT versus NSE methods. The parameters measured were the dominant amplitude, dominant frequency, and mean spectral profile.
Results: At all time resolutions, the error in detecting the frequency of the repeating electrogram pattern was less for NSE than for DFT ($p < 0.001$). The DFT was accurate to 2 s time resolution/0.5 Hz frequency resolution, while the NSE was accurate to 0.5 s time resolution/0.05 Hz frequency resolution. At all time resolutions, significant differences in the dominant amplitude spectral parameter for paroxysmal versus persistent CFAE were greater using NSE than DFT ($p < 0.0001$). For three of five time resolutions, the NSE had greater significant differences than DFT for discriminating the dominant frequency and mean spectral profile parameters between AF types.
Conclusions: The results suggest that the NSE has improved performance versus DFT for measurement of CFAE spectral properties.

1. Introduction

Complex fractionated atrial electrograms (CFAE) are generally recorded with a bipolar contact electrode, and contain either multiple deflections without interruption, a baseline perturbation with continuous deflection, or a cycle length ≤ 120 ms that include isoelectric intervals between deflections [1]. Recently it has been suggested that CFAE can be useful to detect and localize arrhythmogenic regions in atrial fibrillation (AF) patients, with the potential to guide radiofrequency catheter ablation for prevention of arrhythmia recurrence [1,2]. Alternatively, widespread ablation of CFAE may have a debulking effect, reducing the overall arrhythmia substrate [3]. These conflicting possibilities suggest the need to characterize more completely the morphologic and frequency content of CFAE. In patients with short paroxysmal episodes of AF, CFAE morphology as measured by the amplitude, slope, and width of electrogram deflections, and by linear prediction, tends to be highly variable, as compared with electrograms acquired from patients with longstanding persistent AF [4,5]. Similarly, the frequency spectra of CFAE from paroxysmal AF patients appear more random as compared with CFAE from persistent AF [6]. Although both time and frequency domain methods have therefore been helpful to characterize the AF substrate, they do not necessarily have equal robustness. When electrogram amplitude varies randomly, time-domain methods lose performance, while frequency-domain methods remain stable [7]. Therefore spectral analysis may have special efficacy for characterizing these signals.

* Corresponding author. Tel.: +1 212 305 5447; fax: +1 212 342 0447.
E-mail address: ciaccio@columbia.edu (E.J. Ciaccio).

Recent work has suggested that ablation of high dominant frequency (DF) areas may be assistive in preventing AF reinduction in both paroxysmal and persistent AF patients [8]. Although it is desirable to measure high DF components in order to target arrhythmogenic regions, such components are often quasi-periodic and exhibit phase jitter and drift [9]. Furthermore, there can be subtle changes in frequency, on the order of 0.1 Hz, depending upon recording location and type of intervention [10,11]. The frequency resolution of the discrete Fourier transform (DFT), commonly used for analysis of atrial electrograms, is dependent upon *rate/time interval*. For the 1 kHz sampling rate and 8 s interval that is typical for analysis of atrial electrogram sequences [12], the DFT frequency resolution is 0.125 Hz. At this time and frequency resolution, measurement of subtle properties of atrial electrograms can be inaccurate. In this study, a novel spectral estimator (NSE) with frequency resolution dependent upon *rate/period²* is compared to the DFT by measuring electrogram spectral properties. We hypothesized that the NSE would provide improved time resolution while maintaining satisfactory frequency resolution for computation of CFAE spectral parameters.

2. Method

2.1. Clinical data acquisition

Atrial electrograms were recorded in 19 patients referred to the Columbia University Medical Center cardiac electrophysiology laboratory for catheter ablation of AF. Acquisition of electrogram recordings was approved by the Institutional Review Board and they were analyzed retrospectively for this study. Nine patients had clinical paroxysmal AF with normal sinus rhythm as their baseline cardiac rhythm. AF was induced by burst pacing from the coronary sinus or from the right atrial lateral wall, and continued for at least 10 min prior to data collection. Ten other patients had longstanding persistent AF without interruption for several months to many years prior to catheter mapping and ablation. Bipolar atrial mapping was performed using a NaviStar ThermoCool catheter, 7.5F, 3.5 mm tip, with 2 mm spacing between bipoles (Biosense-Webster Inc., Diamond Bar, CA, USA). Electrograms were acquired using the General Electric CardioLab system (GE Healthcare, Waukesha, WI), and filtered at acquisition from 30–500 Hz with a single-pole bandpass filter to remove baseline drift and high frequency noise. The filtered signals were sampled at 977 Hz and stored. Although the bandpass high end was slightly above the Nyquist frequency, negligible signal energy resides in this range [13]. Only signals identified as CFAE by two cardiac electrophysiologists were included for retrospective analysis. CFAE recordings were obtained from two sites outside the ostia of each of the four pulmonary veins. Recordings were also obtained at two left atrial free wall sites, one in the mid-posterior wall, and another on the anterior ridge at the base of the left atrial appendage.

2.2. CFAE data structure

A total of 204 recording sequences of length greater than 16 s, acquired from both paroxysmal and longstanding persistent AF patients, and all meeting the criteria for CFAE, were selected for analysis. DFT and NSE power spectra were computed in the standard electrophysiologic frequency range from 3–12 Hz. The time windows over which spectra were calculated were 8192, 4096, 2048, 1024, and 512 sample points (approximately 8s, 4s, 2s, 1s, and 0.5 s). Binary step changes in window length were used so as to be maximally compatible with the DFT method. The upper limit of 8192 points is considered the optimal time window [12]. The lower limit of 512 sample points is the theoretical minimum to analyze 3 Hz content,

which has a period of 977 samples per second/3 per second=325 sample points for this data. The next binary step at 256 sample points would not extend the entire period of 3 Hz frequency content. Rectangular windowing was used to extract segments for analysis, as unlike other window functions, it does not diminish frequency resolution [14]. For the DFT calculation, the 4096, 2048, 1024, and 512 sample point analysis windows were padded with zeros to 8192 points. For conformity, all DFT and NSE analyses were done using the same 8192 sample point intervals of data. Thus, at the 4096 time resolution level, spectra were generated for two successive 4096 point windows and then averaged, and similarly four 2048 point windows, eight 1024 point windows, and sixteen 512 point windows were averaged for the 2048, 1024, and 512 time resolution levels, respectively.

2.3. Digital power spectra

The DFT power spectrum was constructed using a radix-2 implementation [15]. The NSE power spectrum was constructed as follows [13]. In all equations, underscore denotes a vector, a capital letter signifies a matrix, and the first subscript gives the dimensionality of the vector or matrix. A vector $\underline{e}_w$ of dimension $w \times 1$ was calculated by averaging n successive segments of an $N \times 1$ dimensional signal $\underline{x}_N$, where $\underline{x}_N$ is a CFAE signal normalized to mean zero and unity variance prior to analysis. Each segment $\underline{x}_{w,\,i}$ of this signal, of dimension $w \times 1$, is used for averaging:

$$\underline{e}_w = \frac{1}{n}\sum_i \underline{x}_{w,i}, \quad i=1 \text{ to } n \tag{1}$$

where:

$$\underline{x}_N = \begin{bmatrix} \underline{x}_{w,\,1} \\ \underline{x}_{w,\,2} \\ \vdots \\ \underline{x}_{w,\,n} \end{bmatrix} \tag{2}$$

The process described by Eqs. (1) and (2) is illustrated in Fig. 1. A selected CFAE, signal $\underline{x}$, is graphed from discrete sample point 1 to 1000. Let $w=250$ sample points. Segments $i=1–4$ are noted below $\underline{x}$, and they are the signal segments $\underline{x}_{w,i}$ for $w=250$. When the four segments shown are averaged together, the result is depicted at the bottom of the figure. Any periodicity at $w=250$ will be reinforced in the sum, while random components will diminish. Even in the presence of phase jitter, quasi-periodic components will be reinforced [16]. For a signal $\underline{x}_N$ of length N, the total number of signal segments, and therefore the total number of summations used for
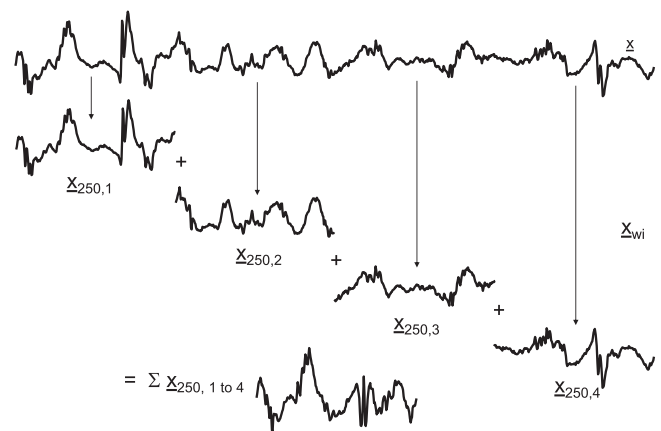
Fig. 1. Process of segment extraction and addition using a complex fractionated atrial electrogram. When the separate segments of length w are added, the result of summation is shown by the trace at the bottom of the figure.

ensemble averaging is given by

$$n = \text{int} \frac{N}{w} \tag{3}$$

with 'int' being the integer function (the real number is rounded down). From Eqs. 1–3, the ensemble average for any segment length w can be written in compact form

$$\underline{e}_w = \frac{1}{n} \cdot U_{w \times N} \cdot \underline{x}_N \tag{4}$$

where:

$$U_{w \times N} = \begin{bmatrix} I_{w \times w} & I_{w \times w} & \cdots & I_{w \times w} \end{bmatrix} \tag{5}$$

with $U_{w \times N}$ being a $w \times N$ dimensional summing matrix and $I_{w \times w}$ are $w \times w$ dimensional identity submatrices used to extract the signal segments from $\underline{x}_N$. Identity matrices are sparse, and the total number of nonzero summations from Eqs. (4) and (5) are n, not N, as in Eq. (1); hence the scale term is $1/n$ in this equation. From Eq. 3, if N/w is not an integer, then the right edge of $U_{w \times N}$ is padded with 0s [13].

The relationship between segment length w used for averaging, which is a period, and frequency f is given by

$$f = \frac{sample\ rate}{w} \tag{6}$$

For any particular segment length w, the power in the ensemble average is

$$P_w = \frac{1}{w} \cdot \underline{e}_w^T \cdot \underline{e}_w \tag{7a}$$

$$P_w = \frac{1}{n^2 w} \sum_i \sum_j \underline{x}_{w,i}^T \cdot \underline{x}_{w,j} \quad i = 1 \text{ to } n, \ j = 1 \text{ to } n \tag{7b}$$

$$P_w = \frac{1}{nN} \cdot \underline{x}_N^T \cdot U_{N \times w} \cdot U_{w \times N} \cdot \underline{x}_N \tag{7c}$$

for signal segments $\underline{x}_{w,i}$ and $\underline{x}_{w,j}$, where the transpose of the summing matrix is given by

$$U_{w \times N}^T = U_{N \times w} \tag{8}$$

Eq. (7a) is based upon the definition of power—it is the sum of squares of each element of $\underline{e}_w$ divided by the total number of such summations w. Eq. (7b) results from substituting Eq. (1) into Eq. (7a), and Eq. (7c) results from substituting Eq. (4) into Eq. (7a). Eq. (7b) is similar to computing the average of the estimated autocorrelation function for all lags $1w$, $2w$, ..., nw, which is given by

$$rav(w) = \frac{1}{nN} \sum_k \underline{x}_N^T \cdot \underline{x}_{N,\phi = k \cdot w} \quad k = 1 \text{ to } n \tag{9a}$$

$$rav(w) = \frac{1}{n^2 w} \sum_k \sum_i \underline{x}_{w,i}^T \cdot \underline{x}_{w,i+k} \quad i = 1 \text{ to } n, \quad k = 1 \text{ to } n \tag{9b}$$

where $\underline{x}_{N,\phi = k \cdot w}$ is shifted in phase from $\underline{x}_N$ by $\phi = k \cdot w$ and Eq. 9b is computed over an interval $2N$. In Fig. 2, an example CFAE is shown in the top graph, and lags in its autocorrelation function are shown in the lower graph when using $w = 125$ sample points ($f = 7.8$ Hz) for illustration. The value of the autocorrelation function at all lags $1w$, $2w$, ..., nw, is averaged to form $rav(w)$ in Eq. (9a) and (9b). Short segments $\underline{x}_{w,i}$ in Eq. (9b) are considered as a first approximation to be mean zero and unity variance, so that the autocorrelation and autocovariance functions were considered to be equivalent and could be used interchangeably. To implement Eq. (9a) in computer software, the following line of software code can be used

$$rav(w) = rav(w) + x(i) \cdot x(i+kw) \quad i = 1 \text{ to } N, \ k = 1 \text{ to } n \tag{10}$$
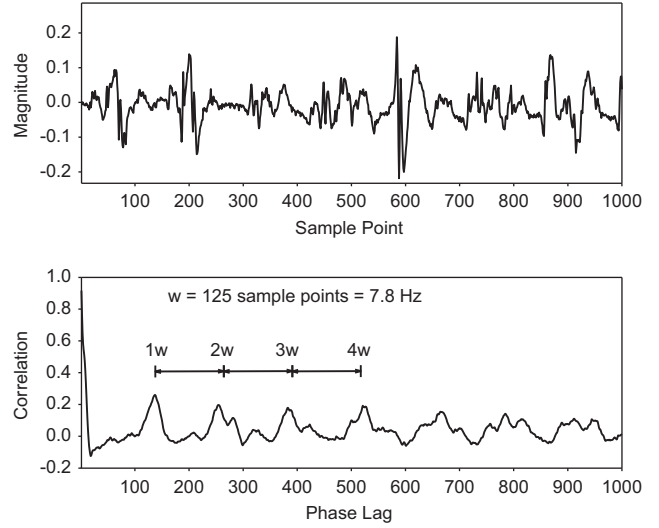
Fig. 2. Autocorrelation function at lags. Top panel: CFAE signal. Lower panel: autocorrelation function with a lag of 125 sample points.

where $x(i)$ is a discrete sample point, and $x(i + kw)$ is a sample point shifted by kw for lags $1w$, $2w$, ..., nw,. This spectral estimator would then be plotted as $rav(w)/N$ versus the frequency $f = sample\ rate/w$. For completeness, in the Appendix it is shown that the mean squared error function is equivalent to the auto-correlation function as a spectral estimator.

In the above derivation, the NSE power spectrum was formed by modeling the signal autocorrelation function. Like the NSE estimator, the DFT power spectrum is also formed by modeling the signal autocorrelation function. Based on the Wiener–Khinchin theorem, the power spectrum of signal $\underline{x}_N$ is given by the Fourier transform of its autocorrelation function

$$S(f) = \frac{1}{N} \sum_\phi (\underline{x}_N \cdot \underline{x}_{N,\phi}) e^{-2\pi j f \phi} \tag{11a}$$

$$S(f) = \frac{1}{nw} \sum_i \sum_w (\underline{x}_{w,i}^T \cdot \underline{x}_{w,i+1}) e^{-2\pi j f w} \quad i = 1 \text{ to } n \tag{11b}$$

where S is the power spectral density, $\underline{x}_N \cdot \underline{x}_{N,\phi}$ is the autocorrelation function with lag ϕ, and Eq. 11b is similar to Eq. (9a) and (9b) for one lag ($k = 1$), with lag symbol ϕ being replaced by w, and with $nw = N$. The DFT power spectral density calculation thus models the autocorrelation function by sinusoidal decomposition. While the DFT incorporates a general basis that is sinusoidal, the NSE basis is data-driven. To show this, signal $\underline{x}_N$ can be projected into NSE space using the following $N \times N$ transformation matrix [13]

$$T_{N \times N}(w) = U_{N \times w} \cdot U_{w \times N} \tag{12}$$

$$= \begin{bmatrix} I_w & I_w & \dots & I_w \\ I_w & I_w & \dots & I_w \\ \vdots & & & \\ I_w & I_w & \dots & I_w \end{bmatrix}$$

Signal $\underline{x}_N$ can then be decomposed using the linear transformation

$$\underline{a}_N(w) = \frac{1}{n} T_{N \times N}(w) \cdot \underline{x}_N \tag{13}$$

where $\underline{a}_N(w)$ are a set of basis vectors of dimension $N \times 1$. The orthogonality of any two basis vectors with periods $w = y$ and $w = z$ is given by

$$\frac{\underline{a}_N^T(y) \cdot \underline{a}_N(z)}{\sqrt{[\underline{a}_N^T(y) \cdot \underline{a}_N(y)][\underline{a}_N^T(z) \cdot \underline{a}_N(z)]}} = \cos \theta \tag{14}$$

where from Eq. (13), the numerator in Eq. (14) can be rewritten as

$$\underline{a}_N^T(y) \cdot \underline{a}_N(z) = \frac{1}{n(y)n(z)} \underline{x}_N^T \cdot T_{T \times N}(y) \cdot T_{N \times N}(z) \cdot \underline{x}_N \tag{15}$$

and $n(y)$ and $n(z)$ are values of n (Eq. (3)) for $w = y$ and $w = z$. As the angle $\theta \to 90°$ (left-hand-side in Eq. (14)$\to 0$) it is indicative of more nearly orthogonal vectors. Orthogonality is exact when $\underline{a}_N^T(y) \cdot \underline{a}_N(z) = 0$ (Eq. (14)), or equivalently when the inner product of each row in $T_{N \times N}(y)$ with the corresponding column in $T_{N \times N}(z)$ equals zero (Eq. (15)). Orthogonality is approximate when y and z have a distant integer relationship over N, so that $\underline{a}_N^T(y) \cdot \underline{a}_N(z)$ in Eq. (14), and the inner products of corresponding rows and columns of $T_{T \times N}(y)$ and $T_{N \times N}(z)$ in Eq. (15) are small but nonzero.

The transformation matrix $T_{N \times N}(w)$ in Eqs. (12) and (13) acts to decompose the signal into periodic ensemble averages. An example is shown in Fig. 3. The CFAE is from the posterior left atrial free wall in a persistent AF patient (panel A). The NSE spectrum is shown in panel B. The DF, which is the tallest fundamental spectral peak in the range of interest [17,18], occurs at 7.08 Hz ($w = 138$ for 977 Hz sampling rate), noted by *. A minimum point at 7.29 Hz ($w = 134$) is noted by **. The basis vector $\underline{a}_N(w)$ from Eq. 13, consisting of repeated ensemble averages, is shown in panel C for the DF, while for the minimum point at ** it is shown in panel D to the same scale. There is substantial power in the basis vector of panel C, because it aligns with CFAE deflections (panel A), while there is much less power in the basis vector of panel D.

2.4. NSE frequency resolution

The frequency resolution of the NSE for any particular segment length $w = k$, where k is an integer, can be described as:

$$fr(k) = \frac{rate}{k} - \frac{rate}{k+1} \tag{16}$$

Eq. 16 can be rewritten as:

$$
\begin{aligned}
fr(k) &= rate \cdot \left(\frac{1}{k} - \frac{1}{k+1} \right) \\
&= rate \cdot \left(\frac{1}{k^2 + k} \right)
\end{aligned}
\tag{17}
$$

For $w = k$ large

$$fr(w) \approx \frac{rate}{w^2} \tag{18}$$

Thus the NSE frequency resolution is proportional to $rate/period^2$. It improves as the period $w = k$ increases (smaller value of $fr(w)$), i.e., at lower frequency values. The NSE estimator contains a maximum of $N/2$ spectral points (an average must contain at least two segments), the same as for the DFT. Therefore the NSE and DFT estimators have equal frequency resolution overall. Although time duration does not directly affect the NSE frequency resolution (Eq. (18)) it may indirectly affect resolution, because as time duration diminishes, the number of signal segments n from Eq. (3) used to form the ensemble average estimate decreases. The cruder estimate would be anticipated to somewhat diminish accuracy.

2.5. Improved NSE time resolution

It was hypothesized that by forming the ensemble average estimate from longer intervals, and then projecting the estimate onto shorter data intervals, the NSE time resolution could be extended. From Eq. (7a)–(7c), the approximate power over a time duration consisting of a reduced number of signal segments $\ell < n$ is given by

$$
\begin{aligned}
\langle P_w \rangle &= \frac{1}{w \cdot \ell} \sum_i (\underline{e}_w^T \cdot \underline{x}_{w,i}), \quad i = 1 \text{ to } \ell < n \\
&= \frac{1}{w \cdot \ell} \underline{e}_w^T \sum_i \underline{x}_{w,i}, \quad i = 1 \text{ to } \ell < n
\end{aligned}
\tag{19}
$$
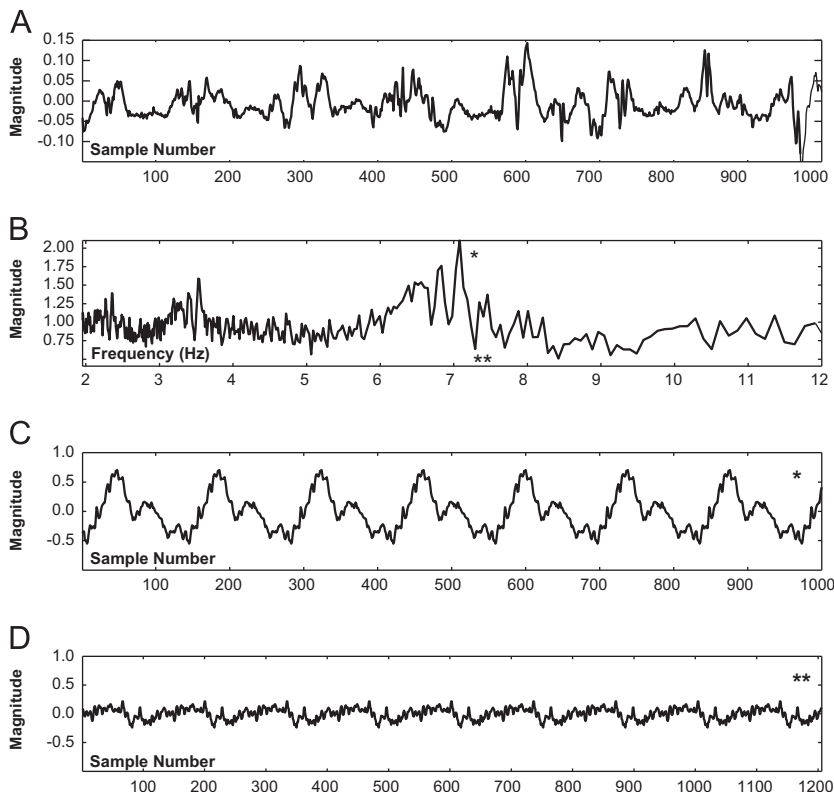
Fig. 3. Construction of basis vectors using the NSE transform. *—the basis vector for the dominant frequency. **—the basis vector for a minimum point on the spectrum. The dominant frequency basis vector (panel C) is of much larger amplitude and therefore greater power as compared with the basis vector for the minimum point (panel D).

Using Eq. (19), the local frequency content, which is estimated from the average computed over ℓ segments, is compared to the global frequency content, i.e., the ensemble average $\underline{e}_w$ computed over n segments. In this study, using ensemble averages computed from 2048 points, power spectra were estimated for $\ell = 1024$ and $\ell = 512$ points using Eq. (19).

2.6. Comparison of estimators using repeating electrogram patterns

For comparison of NSE versus DFT spectral estimators, a repetitive electrogram pattern was constructed. The pattern was extracted from a CFAE at a random point and with random window size, and adjusted to mean zero and a standard deviation of 0.08, which is on the order of $2\times$ the average standard deviation of the CFAE signals acquired for this study prior to their normalization. The pattern was then repeated to a total length of $N = 8192$ discrete sample points. The 204 CFAE themselves were used as interference having unknown frequency content, by adding the repeating electrogram pattern to each CFAE. It was determined whether the frequency of the repeating electrogram pattern could be detected as the DF in the power spectrum of the resulting signal. Jitter was also introduced by randomly shifting each repeating electrogram pattern by up to ± 5 sample points (approximately ± 5 ms) to simulate phase noise. The DF was measured for 20 different electrogram patterns with phase noise using the DFT and NSE spectral estimators. Estimates were considered satisfactory when the absolute error was less than 0.5 Hz.

Examples of a repeating electrogram pattern added to a CFAE are shown in Fig. 4. The top panel is graphed with sample points 1–500 of a CFAE from the left superior pulmonary vein ostium in a persistent AF patient (black trace). Overlapping it is the same CFAE with a repeating electrogram pattern added having a period of approximately 170 sample points or 5.75 Hz in frequency (red trace). The cycles of repeating pattern are labeled from a–d at the large downward deflection, which is a prominent fiducial point. These downward deflections change from one cycle to the next due to the level of interference from the added CFAE. The horizontal arrows show equal intervals along the traces. The repeating pattern has been shifted by random jitter in segment b–c versus segment c–d, so that the periods between b–c and c–d are unequal. The cycle length of b–c is longer than c–d. In the lower panel of Fig. 4, a CFAE from the left superior pulmonary vein ostium in a paroxysmal AF patient is graphed from
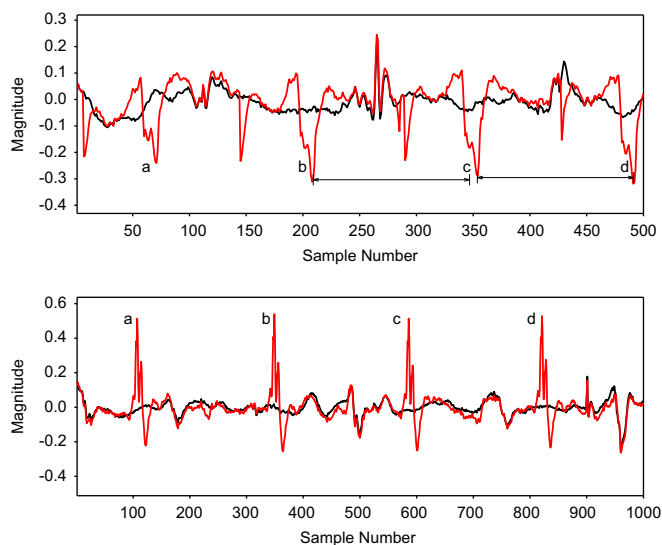
sample points 1–1000. Overlapping it in red is a repeating electrogram pattern, this time having a period of approximately 250 sample points or 4 Hz in frequency, with the CFAE acting as interference. Here again, as in the top panel, cycles a–d are unequal in length due to the phase jitter introduced to the repeating electrogram pattern. For 20 trials, the error was calculated as the absolute difference in the DF measured from the power spectrum versus the actual frequency of the repeating electrogram pattern. Significant differences in mean error values for DFT versus NSE measurements were determined using the paired t-test (SigmaPlot 2004 for Windows Ver. 9.01, Systat Software, Chicago) at the $p < 0.05$ level.

2.7. Real data comparison of the spectral estimators

Three spectral properties were measured from the real data to compare the DFT versus NSE spectral estimators [6]. The dominant frequency (DF), which is reflective of the atrial activation rate [10,11], was determined in the physiologic range of interest, 3–12 Hz [16]. The second spectral property that was measured was the dominant amplitude (DA), defined as the amplitude of the dominant spectral peak [6]. It is proportional to the power contained in the fundamental frequency component of the signal, and therefore to the proportion of tissue undergoing electrical activation at the cycle length given by the DF. The third measurement, the mean spectral magnitude (MP), reflects the characteristics of all frequency components rather than just the dominant frequency [6]. The MP is related to the noise floor, which itself is dependent upon the degree of randomness in the electrical activation pattern. Measurements were made at time resolutions of 8 s, 4 s, 2 s, 1 s, and 0.5 s.

The DA, DF, and MP were measured and compared for paroxysmal versus persistent CFAE recordings. In accord with prior analyses [6], for the MP measurement, recordings from all locations were compared (114 persistent and 90 paroxysmal CFAE). Also in accord with prior analyses [6], for the DA and DF measurements, only recordings from the pulmonary vein ostia were compared (76 persistent and 60 paroxysmal CFAE recordings). The DF was detected automatically in computer software as the tallest spectral peak in the range 3–12 Hz, excluding harmonics. The unpaired t-test was used to compare the means of paroxysmal versus persistent AF data (MedCalc ver. 9.5, 2008, MedCalc Software bvba, Mariakerke, Belgium), with the $p < 0.05$ level indicating significance.

2.8. Synthetic data comparison of the spectral estimators

As an additional test of the performance of the NSE versus DFT estimators, a synthetic fractionated electrogram was constructed and analyzed. It consisted of three additive components, simple periodic geometrical shapes, with frequencies of 3.26 Hz, 4.77 Hz, and 6.98 Hz. Random noise with a standard deviation of 2.5 millivolts, approximately $50\times$ the standard deviation of the CFAE, was added to the synthetic fractionated electrogram. It was then determined whether or not the three largest peaks in the NSE and DFT spectra in the range 3–12 Hz, excluding harmonics, coincided with the frequencies of the additive synthetic components. This process was repeated for 15 trials with a different random noise used on each trial.

3. Results

In Table 1, the average estimation error for detecting the repeating electrogram pattern over 20 trials is shown for DFT versus NSE spectral estimators. The absolute values are given in Hertz. At all levels from 8192 through 512 sample points of time resolution, the NSE estimator was more accurate than DFT. Thus for the five resolution levels 8 s, 4 s, 2 s, 1 s, and 0.5 s, the error in detecting

Fig. 4. Construction of a synthetic periodic component. (A) Persistent AF. (B) Paroxysmal AF. Black traces—the interference signal. Red traces—repeating electrogram pattern with interference added. (For interpretation of the references to color in this figure legend, the reader is referred to the web version of this article.)

repeating electrogram patterns was significantly less when using the NSE estimator as compared with DFT ($p < 0.001$).

Tables 2–4 show results for detecting differences in power spectral parameters for paroxysmal versus persistent AF. In Table 2, mean values of the DA parameter are shown. At all time resolutions when using the NSE spectrum for calculation, the DA is greater in persistent AF ($p < 0.0001$), indicating that it is often more predominant as compared with other spectral components in the persistent AF spectra, versus paroxysmal AF spectra where the DF is less dominant. In Table 3, the mean DF is higher in persistent as compared with paroxysmal AF for all data. The significance level is higher for NSE at the 8192, 1024, and 512 levels and is similar in NSE and DFT at the 4096 and 2048 levels. In Table 4, the mean MP is larger in paroxysmal as compared with persistent AF for all data. There is a greater significant difference for the NSE method at the 2048, 1024, and 512 levels. The DFT and NSE estimators have similar significant differences at the 8192 and 4096 levels ($p < 0.0001$). The larger DA, higher DF, and lower MP in persistent as compared with paroxysmal AF data are in accord with the known properties of both types of AF, i.e., persistent AF activation patterns tend to be more regular and stable, and have a faster rate as compared with paroxysmal AF activation patterns [4,5,16].

Fig. 5A shows the synthetic geometric shapes used to test the NSE and DFT estimators. At the top of the panel are the individual shapes, shown offset. At the bottom of the panel is the combined synthetic pattern. Fig. 5B shows the NSE and DFT spectra for the noiseless synthetic fractionated electrogram. For reference, the frequencies of the individual components are shown as vertical lines. The highest spectral peaks coincide with the actual synthetic component frequencies for both estimators. For both estimators, there is also a tall harmonic peak—the second harmonic of the 3.26 Hz component, which is labeled. For the DFT estimator, the 3.26 Hz and 4.77 Hz frequency peaks are slightly misaligned while for the NSE estimator, the 6.98 Hz peak is slightly misaligned. Overall, the top three spectral peaks in the range 3–12 Hz, excluding harmonics, coincided with the three synthetic components in 14/15 trials for the NSE estimator, and for 9/15 trials for the DFT estimator. An example is shown in Fig. 6. The top three peaks excluding harmonics coincide with the synthetic component frequencies for the NSE spectrum (panel A). Only two of the top three peaks excluding harmonics coincide with the synthetic component frequencies for the DFT spectrum (panel B), where again the actual frequencies of the synthetic components are denoted with vertical lines for reference.

4. Discussion

4.1. Summary

In the study, details concerning a novel spectral estimator, or NSE, were described. The NSE and DFT estimators were compared to analyze fractionated atrial electrograms acquired from paroxysmal and persistent AF patients. To form the power spectrum, the NSE

Table 1
Error in detecting repeating electrogram pattern (Hz).

Time	DFT	NSE	P
8192	0.285 ± 0.346	0.010 ± 0.019	$P < 0.001$
4096	0.331 ± 0.353	0.032 ± 0.021	$P < 0.001$
2048	0.407 ± 0.413	0.125 ± 0.258	$P < 0.001$
1024	0.537 ± 0.490	0.110 ± 0.062	$P < 0.001$
512	0.896 ± 0.736	0.191 ± 0.223	$P < 0.001$

Error values are given as mean $\pm$ standard deviation in units of Hertz, for analysis time windows of 8192 to 512 sample points (approximately 8 s to 0.5s). P is = the significance level using the paired t-test.

Table 2
Real data—dominant amplitude (millivolts).

Time	Per—DFT	Par—DFT	P	Per—NSE	Par—NSE	P
8192	$0.849+0.375$	$0.688+0.297$	$=0.0074$	$1.842+0.606$	$1.466+0.297$	< 0.0001
4096	$0.567+0.273$	$0.446+0.195$	$=0.0044$	$1.742+0.524$	$1.407+0.258$	< 0.0001
2048	$0.349+0.158$	$0.270+0.104$	$=0.0011$	$1.596+0.391$	$1.310+0.200$	< 0.0001
1024	$0.212+0.098$	$0.161+0.064$	$=0.0007$	$1.137+0.299$	$0.937+0.179$	< 0.0001
512	$0.118+0.051$	$0.104+0.038$	NS	$0.772+0.191$	$0.656+0.131$	$=0.0001$

Per=persistent AF data, Par=paroxysmal AF data, and P=the significance level using the unpaired T-test.

Table 3
Real data—dominant frequency (Hertz).

Time	Per—DFT	Par—DFT	P	Per—NSE	Par—NSE	P
8192	$6.253+0.919$	$5.623+1.126$	$=0.0005$	$6.242+0.905$	$5.563+1.090$	$=0.0001$
4096	$6.275+0.946$	$5.405+1.005$	< 0.0001	$6.188+0.943$	$5.795+1.153$	$=0.0305$
2048	$6.299+1.011$	$5.556+1.304$	$=0.0003$	$6.385+0.958$	$5.913+1.233$	$=0.0132$
1024	$6.177+1.185$	$5.862+1.500$	NS	$5.887+0.946$	$5.524+0.957$	$=0.0288$
512	$6.387+1.311$	$6.116+1.753$	NS	$6.586+1.242$	$6.044+1.425$	$=0.0193$

Per=persistent AF data, Par=paroxysmal AF data, and P=the significance level using the unpaired t-test.

Table 4
Real data—mean spectral profile (millivolts).

Time	Per—DFT	Par—DFT	P	Per—NSE	Par—NSE	P
8192	$0.258+0.071$	$0.305+0.068$	< 0.0001	$0.342+0.105$	$0.405+0.076$	< 0.0001
4096	$0.243+0.072$	$0.285+0.058$	< 0.0001	$0.364+0.102$	$0.428+0.078$	< 0.0001
2048	$0.266+0.074$	$0.306+0.062$	$=0.0001$	$0.386+0.095$	$0.457+0.077$	< 0.0001
1024	$0.340+0.080$	$0.383+0.073$	$=0.0001$	$0.438+0.103$	$0.505+0.080$	< 0.0001
512	$0.432+0.082$	$0.463+0.077$	$=0.0064$	$0.471+0.094$	$0.505+0.063$	$=0.0036$

Per=persistent AF data, Par=paroxysmal AF data, and P= the significance level using the unpaired t-test.
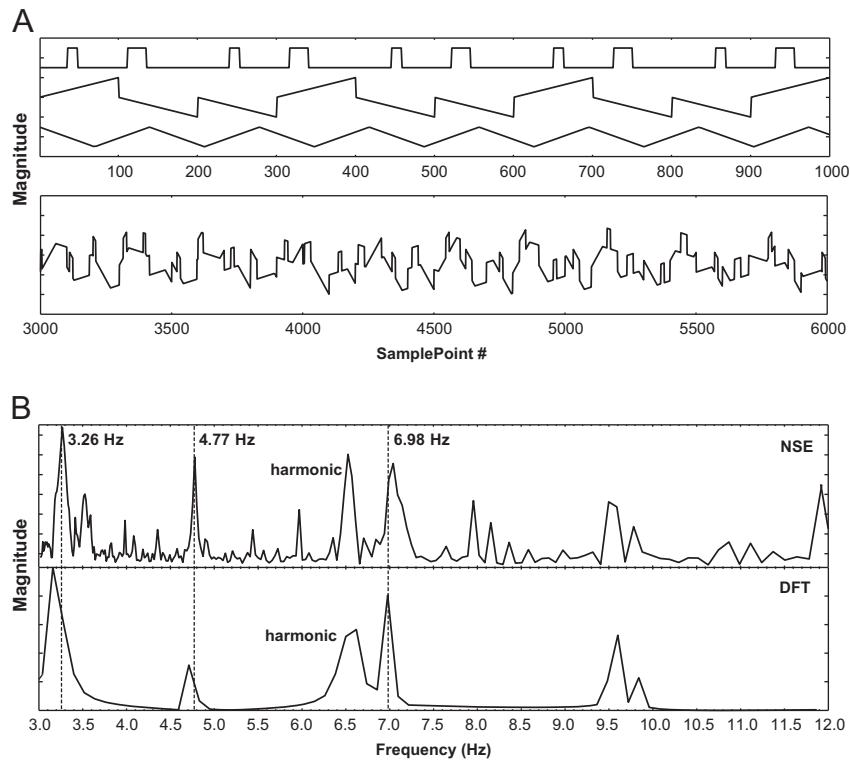
Fig. 5. Construction of the synthetic CFAE from three geometric components. (A). Time series components shown offset and combined. (B). NSE and DFT frequency spectra. Vertical lines denote the frequencies of the three additive components used to construct the synthetic fractionated electrogram.

Fig. 6. Frequency spectra of synthetic fractionated electrogram with three additive components and random noise. (A). NSE spectrum. (B). DFT spectrum. The physiologic range of 3–12 Hz is shown. Vertical lines denote the frequencies of the three additive components used to construct the synthetic fractionated electrogram.

averages the autocorrelation function at lags, while the DFT uses a sinusoidal approximation to model the autocorrelation function. Differences in modeling the autocorrelation function for power spectrum formation contribute to the differing properties of the DFT and NSE estimators. In contrast to the DFT frequency resolution, which is proportional to $rate/time\ duration$, the NSE frequency resolution is proportional to $rate/period^2$. Power spectral equations similar to that of the NSE were derived from the average autocorrelation and mean squared error functions.

The NSE time resolution at 1024 and 512 sample points (1 s and 0.5 s, respectively) was improved using a temporally globalized ensemble average model over 2 s, which was projected onto temporally localized data (Eq. 19). The global model contained local information, which became evident by projection onto the shorter electrogram interval containing localized data. The maximum error in detecting a repeating electrogram pattern was found to be 0.896 ± 0.736 Hz for DFT versus 0.191 ± 0.223 Hz for NSE, which occurred for 0.5 s time windows ($p < 0.001$; Table 1).

The NSE had significantly improved spectral qualities compared with the DFT across the range of time resolutions used for analysis, from 8 s to the theoretical minimum time interval for analysis of 0.5 s (Table 1). The NSE was also more useful to determine significant differences in paroxysmal versus persistent CFAE spectral parameters. The NSE spectra provided the best discrimination of the DA spectral parameter in paroxysmal versus persistent AF as compared with the DFT spectra at all time resolution levels of 8 s, 4 s, 2 s, 1 s, and 0.5 s ($p < 0.0001$). NSE spectra provided the best discrimination of DF and MP spectral parameters at three of five time resolution levels.

4.2. Clinical correlates

In previous work, the DA and MP spectral parameters have been shown to be correlated to the duration of AF in months, and to the left atrial volume of AF patients [6]. The DF spectral parameter has also been shown to be very useful for AF patient evaluation in the electrophysiology laboratory. For example, local reentrant circuits may be indicated by lower DFs that coexist in chaotic AF sequences [19]. Paroxysmal AF, but not persistent AF, can be driven by high DF sources and a left-to-right DF gradient [20]. A significant reduction in DF in both left and right atria, with a loss of the left-to-right atrial gradient after ablation, is associated with a higher probability of maintaining sinus rhythm in both paroxysmal and persistent AF patients [21]. It is also possible to classify paroxysmal as compared with persistent AF by detecting subtle changes in the DF, combined with analysis of an entropy measure [22]. Moreover, there is significant regional variation in the DF in paroxysmal but not persistent AF [5,23].

Although recording intervals of ≥ 2 s are necessary for reliable DF measurement using the DFT, as has been shown in the present study (Table 1) and elsewhere [24], spectral changes preceding major arrhythmic events such as spontaneous termination of paroxysmal atrial fibrillation may occur over intervals shorter than 2 s [25]. The NSE, but not the DFT, would therefore be suited to this purpose, since the time resolution is satisfactory down to the theoretical limit of 0.5 s for the physiologic frequency range of interest (Table 1). Moreover, subtle spatial gradients in DF of a few tenths of Hertz exist away from the pulmonary veins [26], and subtle changes in DF of a few tenths of Hertz caused by pharmacologic agents can also occur [27]. These changes would not be readily measureable in patients using the DFT, which had an error < 0.5 Hz only for window segments of 2 s and greater (Table 1). Conflicting results from DFT spectral analysis of fractionated atrial electrograms may thus be partially explained by the lack of time and frequency resolution. The NSE may therefore be helpful to clarify previous findings.

As wavelet decomposition is not as commonly used for analysis of AF electrograms as compared with the DFT, and as it estimates different spectral properties, it was not used for comparison in the present study. However, wavelet decomposition has been found useful for applications including the automatic detection of local activation times when the pattern of atrial fibrillation is complex [28], for automated description of fractionation morphology in atrial electrograms [29], extraction of the spatiotemporal characteristics in paroxysmal AF to identify arrhythmogenic regions for catheter ablation [30], and to predict the spontaneous termination of paroxysmal AF and the outcome of electrical cardioversion in persistent AF patients [31]. Thus this spectral estimator can potentially provide complimentary information to the DFT and NSE estimators when AF data is analyzed.

Besides application to fractionated atrial electrograms, the NSE algorithm has been implemented for other types of data including the study of ventricular tachyarrhythmia onset [32] and videocapsule image analysis that is used for screening in celiac disease [33].

In recent investigations, the spectral parameters described in this study were used for QRST cancellation [34] and the NSE method was implemented for heart sounds quantification [35]. Similar to the NSE, in a prior study, heart sounds patterns have been detected by averaging segments of the acoustic signal at different lengths w [36]. Based on these investigations, the NSE method may be generalizable to many types of biomedical data.

4.3. Limitations

The NSE spectrum contains subharmonics and cross-terms [6,37]. Such components can interfere with DF detection and can cause the MP parameter to be increased. Second harmonics can be reduced in NSE by imparting antisymmetry to the ensemble averages [6,37], but this can diminish the power of pertinent frequency components as well. To further reduce subharmonics and cross-terms, higher-order harmonics should be canceled [37], the subject of future study. Although as shown in the present study, the NSE method can account for inexact periodicity (phase noise), other methods to measure frequency content under such conditions may also be helpful to analyze fractionated atrial electrograms [38,39]. In paroxysmal AF patients, the DF is related to the degree of fractionation [40]. Therefore the DA and MP spectral parameters may be in part dependent on the DF.

5. Conclusions

In the presence of interference and phase noise, a repeating electrogram pattern was found to be accurately detected to the theoretical minimum time resolution of 0.5 s using the NSE estimator. At all time resolution levels, the NSE method had negligible bias and significantly reduced variance as compared with the DFT estimator (Table 1). The NSE method was also found useful to determine significant differences in the DA, DF, and MP spectral parameters in paroxysmal versus persistent CFAE data. Based on both the reduced estimation error in detecting a repeating pattern, and the greater significant differences in real paroxysmal versus persistent AF spectral parameters, the NSE estimator may be useful for frequency analysis of atrial signals as a comparative technique with respect to the traditional DFT method, and to validate the results of the DFT. The NSE may even be useful to provide improved frequency analysis of CFAE data at short time resolutions, but this should be tested in a prospective study with larger sample size.

The findings of this study suggest that the NSE method can provide improved time resolution, which along with the better frequency resolution [14], can result in more accurate measurement of spectral properties in fractionated atrial electrogram recordings. At the 0.5 s time resolution level, the error was still below 0.5 Hz for the NSE estimator (Table 1). Regardless of time window, the frequency resolution of NSE averages 0.05 Hz in the 3–12 Hz physiologic frequency band [14]. This compares with a best time resolution of 2 s for DFT found in this study (Table 1) and elsewhere [24], which at a sampling rate of 1k Hz corresponds to a 0.5 Hz frequency resolution. As the NSE technique is automated without the need for manual correction, user bias is eliminated, with no need for *ad hoc* parameterization and input of *a priori* information, so that it is potentially applicable to real-time analysis in the clinical electrophysiology laboratory for evaluation of AF patients.

Conflicts of interest statement

Appendix

5.1. Mean Squared Error as Alternative to Autocorrelation Function for Spectral Estimation

The mean squared error (MSE) between a signal $\underline{x}_N$ and its lagged version $\underline{x}_{N,\phi}$ is approximated by

$$MSE \approx (\underline{x}_N - \underline{x}_{N,\phi})^T \cdot (\underline{x}_N - \underline{x}_{N,\phi}) \tag{A1}$$

where the right-hand-side in Eq. A1 is divided by the vector length. If signal statistics are approximately stationary then

$$(\underline{x}_{N,\phi}^T \cdot \underline{x}_{N,\phi}) \sim (\underline{x}_N^T \cdot \underline{x}_N) \tag{A2}$$

From. Eqs. A1 and A2:

$$MSE \approx (\underline{x}_N^T \cdot \underline{x}_N) - (\underline{x}_N^T \cdot \underline{x}_{N,\phi}) - (\underline{x}_{N,\phi}^T \cdot \underline{x}_N) + (\underline{x}_{N,\phi}^T \cdot \underline{x}_{N,\phi})$$
$$\approx 2(\underline{x}_N^T \cdot \underline{x}_N) - 2(\underline{x}_N^T \cdot \underline{x}_{N,\phi}) \tag{A3}$$

For segments $\underline{x}_{w,i}$ having length w and segment number i, and switching the lag variable from ϕ to w

$$MSE \approx 2(\underline{x}_N^T \cdot \underline{x}_N) - 2\sum_i \underline{x}_{w,i}^T \cdot \underline{x}_{w,i+1} \quad i = 1 \text{ to } n \tag{A4}$$

Eq. (A4) is similar to Eq. (9B) when $k = 1$. By replacing the index $i+1$ with $i+k$, $k = 1$ to n in Eq. (A4), the average for all lags $1w$, $2w$, … nw is obtained, which can be plotted as an inverted version of the average autocorrelation power spectrum (Eq. (9B)).

References

[1] K. Nademanee, J. McKenzie, E. Kosar, M. Schwab, B. Sunsaneewitayakul, T. Vasavakul, C. Khunnawat, T. Ngarmukos, A new approach for catheter ablation of atrial fibrillation: mapping of the electrophysiologic substrate, J. Am. Coll. Cardiol. 43 (2004) 2044–2053.

[2] K. Nademanee, M.C. Schwab, E.M. Kosar, M. Karwecki, M.D. Moran, N. Visessook, A.D. Michael, T. Ngarmukos, Clinical outcomes of catheter substrate ablation for high-risk patients with atrial fibrillation, J. Am. Coll. Cardiol. 51 (2008) 843–849.

[3] C.S. Elayi, A. Verma, L. Di Biase, C.K. Ching, D. Patel, C. Barrett, D. Martin, B. Rong, T.S. Fahmy, Y. Khaykin, R. Hongo, S. Hao, G. Pelargonio, A. Dello Russo, M. Casella, P. Santarelli, D. Potenza, R. Fanelli, R. Massaro, M. Arruda R.A. Schweikert, A. Natale, Ablation for longstanding permanent atrial fibrillation: results from a randomized study comparing three different strategies, Heart Rhythm 5 (2008) 1658–1664.

[4] E.J. Ciaccio, A.B. Biviano, W. Whang, A. Gambhir, H. Garan, Different characteristics of complex fractionated atrial electrograms in acute paroxysmal versus long-standing persistent atrial fibrillation, Heart Rhythm 7 (2010) 1207–1215.

[5] E.J. Ciaccio, A.B. Biviano, W. Whang, A. Gambhir, A.J. Einstein, H. Garan, Differences in repeating patterns of complex fractionated left atrial electrograms in longstanding persistent as compared with paroxysmal atrial fibrillation, Circ. Arrhythmia .Electrophysiol. 4 (2011) 470–477.

[6] E.J. Ciaccio, A.B. Biviano, W. Whang, A. Gambhir, H. Garan, E.J. Ciaccio, A.B. Biviano, W. Whang, A. Gambhir, H. Garan, Spectral profiles of complex fractionated atrial electrograms are different in longstanding and acute onset atrial fibrillation atrial electrogram spectra, J. Cardiovasc. Electrophysiol. 23 (2012) 971–979.

[7] K.R. Grzeda, S.F. Noujaim, O. Berenfeld, J. Jalife, Complex fractionated atrial electrograms: properties of time-domain versus frequency-domain methods, Heart Rhythm 6 (2009) 1475–1482.

[8] Koji Kumagai, Tamotsu Sakamoto, Keijiro Nakamura Suguru Nishiuchi, Mamoru Hayano, Tatsuya Hayashi, Takehito Sasaki, Kazutaka Aonuma Shigeru Oshima, Combined dominant frequency and complex fractionated atrial electrogram ablation after circumferential pulmonary vein isolation of atrial fibrillation, J. Cardiovasc. Electrophysiol. (2013), http://dx.doi.org/10.1111/jce.12166.

[9] J.W. Jarman, T. Wong, P. Kojodjojo, H. Spohr, J.E. Davies, M. Roughton, D.P. Francis, P. Kanagaratnam, V. Markides, D.W. Davies, N.S. Peters, Spatiotemporal behavior of high dominant frequency during paroxysmal and persistent atrial fibrillation in the human left atrium, Circ. Arrhythm Electrophysiol. 5 (2012) 650–658.

[10] J. Ng, A.H. Kadish, J.J. Goldberger, Effect of electrogram characteristics on the relationship of dominant frequency to atrial activation rate in atrial fibrillation, Heart Rhythm 3 (2006) 1295–1305.

[11] J. Ng, R.S. Passman, R. Arora, A.H. Kadish, J.J. Goldberger, Paradoxical change in atrial fibrillation dominant frequencies with baroreflex-mediated parasympathetic stimulation with phenylephrine infusion, J. Cardiovasc. Electrophysiol. 23 (2012) 1045–1050.

[12] A.B. Biviano, W. Bain, W. Whang, J. Leitner, J. Dizon, K. Hickey, H. Garan, Focal left atrial tachycardias not associated with prior catheter ablation for atrial fibrillation: clinical and electrophysiological characteristics, Pacing Clin. Electrophysiol. 35 (2012) 17–27.

[13] E.J. Ciaccio, A.B. Biviano, W. Whang, J. Coromilas, H. Garan, A new transform for the analysis of complex fractionated atrial electrograms, BioMed Eng OnLine 10 (2011) 35–45.

[14] E.J. Ciaccio, A.B. Biviano, W. Whang, A. Gambhir, H. Garan, Improved frequency resolution for characterization of complex fractionated atrial electrograms, BioMed. Eng. OnLine 11 (2012) 17.

[15] W.H. Press, S.A. Teukolsky, W.T. Vetterling, B.P. Flannery, Numerical Recipes in Fortran, Cambridge University Press, New York (1992) 542–550.

[16] E.J. Ciaccio, A.B. Biviano, W. Whang, A.L. Wit, J. Coromilas, H. Garan, Optimized measurement of activation rate at left atrial sites with complex fractionated electrograms during atrial fibrillation, J. Cardiovasc. Electrophysiol. 21 (2010) 133–143.

[17] G.W. Botteron, J.M. Smith, A technique for measurement of the extent of spatial organization of atrial activation during atrial fibrillation in the intact human heart, IEEE Trans. Biomed. Eng. 42 (1995) 579–586.

[18] E.J. Ciaccio, A.B. Biviano, W. Whang, A.L. Wit, H. Garan, J. Coromilas, New methods for estimating local electrical activation rate during atrial fibrillation, Heart Rhythm 6 (2009) 21–32.

[19] M. Yokokawa, A. Chugh, M. Ulfarsson, H. Takaki, L. Han, K. Yoshida, M. Sugimachi, F. Morady, H. Oral, Effect of linear ablation on spectral components of atrial fibrillation, Heart Rhythm 7 (2010) 1732–1737.

[20] N. Voigt, A. Trausch, M. Knaut, K. Matschke, A. Varro, D.R. Van Wagoner, S. Nattel, U. Ravens, D. Dobrev, Left-to-right atrial inward rectifier potassium current gradients in patients with paroxysmal versus chronic atrial fibrillation, Circ. Arrhythmia Electrophysiol. 3 (2010) 472–480.

[21] F. Atienza, J. Almendral, J. Jalife, S. Zlochiver, R. Ploutz-Snyder, E.G. Torrecilla, A. Arenal, J. Kalifa, F. Fernandez-Aviles, O. Berenfeld, Real-time dominant frequency mapping and ablation of dominant frequency sites in atrial fibrillation with left-to-right frequency gradients predicts long-term maintenance of sinus rhythm, Heart Rhythm 6 (2009) 33–40.

[22] Alcaraz R., Sandberg F., Sornmo L., Rieta J.J. Application of frequency and sample entropy to discriminate long-term recordings of paroxysmal and persistent atrial fibrillation, in: Annual International Conference of the IEEE Engineering in Medicine and Biology Society. 2010, 1, pp. 4558–4561.

[23] M.K. Stiles, A.G. Brooks, P. Kuklik, B. John, H. Dimitri, D.H. Lau, L. Wilson, S. Dhar, R.L. Roberts-Thomson, L. Mackenzie, G.D. Young, P. Sanders, High-density mapping of atrial fibrillation in humans: relationship between high-frequency activation and electrogram fractionation, J. Cardiovasc. Electrophysiol. 19 (2008) 1245–1253.

[24] J. Ng, A.H. Kadish, J.J. Goldberger, Technical considerations for dominant frequency analysis, J. Cardiovasc. Electrophysiol. 18 (2007) 757–764.

[25] H.W. Tso, Y.J. Lin, C.T. Tai, S.A. Chen, T. Kao, Characteristics of fibrillatory activities during spontaneous termination of paroxysmal atrial fibrillation: new insight from high-density right atrium frequency mapping, Can. J. Cardiol. 28 (2012) 87–94.

[26] K. Suenari, Y.J. Lin, S.L. Chang, L.W. Lo, Y.F. Hu, T.C. Tuan, S.Y. Huang, C.T. Tai, Y. Nakano, Y. Kihara, H.M. Tsao, T.J. Wu, S.A. Chen, Relationship between arrhythmogenic pulmonary veins and the surrounding atrial substrate in patients with paroxysmal atrial fibrillation, J. Cardiovasc. Electrophysiol. 22 (2011) 405–410.

[27] J. Ng, R. Villuendas, I. Cokic, J.E. Schliamser, D. Gordon, H. Koduri, B. Benefield, J. Simon, S.N. Murthy, J.W. Lomasney, J.A. Wasserstrom, J.J. Goldberger, G.L. Aistrup, R. Arora, Autonomic remodeling in the left atrium and pulmonary veins in heart failure: creation of a dynamic substrate for atrial fibrillation, Circ. Arrhythmia Electrophysiol. 4 (2011) 388–396.

[28] R.P. Houben N.M. de Groot M.A. Allessie, Analysis of fractionated atrial fibrillation electrograms by wavelet decomposition, IEEE Trans. Biomed. Eng. 57 (2010) 1388–1398.

[29] V. Kremen, L. Lhotská, M. Macas, R. Cihák, V. Vancura, J. Kautzner, D. Wichterle, A new approach to automated assessment of fractionation of endocardial electrograms during atrial fibrillation, Physiol. Meas. 29 (2008) 1371–1381.

[30] J. Zhao, Y. Yao, W. Huang, R. Shi, S. Zhang, I.J. LeGrice, N.A. Lever, B.H. Smaill, Novel methods for characterization of paroxysmal atrial fibrillation in human left atria, Open Biomed. Eng. J. 7 (2013) 29–40.

[31] Alcaraz R., Rieta J.J. Central tendency measure and wavelet transform combined in the non-invasive analysis of atrial fibrillation recordings. Biomed. Eng. Online 2012 11;46.

[32] E.J. Ciaccio, J. Coromilas, A.L. Wit, H. Garan, Onset dynamics of ventricular tachyarrhythmias as measured by dominant frequency, Heart Rhythm 8 (2011) 615–623.

[33] E.J. Ciaccio, C.A. Tennyson, S.K. Lewis, S. Krishnareddy, G. Bhagat, P.H. Green, Distinguishing patients with celiac disease by quantitative analysis of videocapsule endoscopy images, Comput. Methods Programs Biomed. 100 (2010) 39–48.

[34] José Joaquín Rieta Jorge Mateo, Radial basis function neural networks applied to efficient QRST cancellation in atrial fibrillation, Comput. Biol. Med. 43 (2013) 154–163.

[35] H. Naseri, M.R. Homaeinezhad, Detection and boundary identification of phonocardiogram sounds using an expert frequency-energy based metric, Ann. Biomed. Eng. 41 (2013) 279–292.

[36] P.P. Kanjilal, S. Palit, On multiple pattern extraction using singular value decomposition, IEEE Trans. Signal Process. 43 (1995) 1536–1540.

[37] E.J. Ciaccio, A.B. Biviano, H. Garan, Comparison of spectral estimators for characterizing fractionated atrial electrograms, BioMed. Eng. OnLine 12 (2013) 72.

[38] W.A. Sethares, T.W. Staley, Periodicity transforms, IEEE Trans. Signal Process. 47 (1999) 2953–2964.

[39] A. Bauer, J.W. Kantelhardt, A. Bunde, P. Barthel, R. Schneider, M. Malik, G. Schmidt, Phase-rectified signal averaging detects quasi-periodicities in non-stationary data, Physica A 364 (2006) 423–434.

[40] F. Atienza, D. Calvo, J. Almendral, S. Zlochiver, K.R. Grzeda, N. Martínez-Alzamora, E. González-Torrecilla, A. Arenal, F. Fernández-Avilés, O. Berenfeld, Mechanisms of fractionated electrograms formation in the posterior left atrium during paroxysmal atrial fibrillation in humans, J. Am. Coll. Cardiol. 57 (2011) 1081–1092.